Article

Mechanism Insight into Catalytic Performance of $Ni_{12}P_5$ over Ni_2P toward the Catalytic Deoxygenation of Butyric Acid

Shuai Fu [1], Dan Li [2], Tinghao Liu [1], Lijuan Liu [1], Huaqing Yang [1,*] and Changwei Hu [2]

1 College of Chemical Engineering, Sichuan University, Chengdu 610065, China; fushuaibox@163.com (S.F.); tinghao_liu@163.com (T.L.); lljwxl425@163.com (L.L.)
2 Key Laboratory of Green Chemistry and Technology, Ministry of Education, College of Chemistry, Sichuan University, Chengdu 610064, China; danli@scu.edu.cn (D.L.); changweihu@scu.edu.cn (C.H.)
* Correspondence: huaqingyang@scu.edu.cn; Tel.: +86-28-85464466

Abstract: The Ni/P ratio of nickel phosphide has an important effect on the catalytic performance toward the deoxygenation of fatty acids to biofuel. The $Ni_{12}P_5$ cluster is preferred to model $Ni_{12}P_5$ catalyst with butyric acid as the reactant model of palmitic acid. The catalytic deoxygenation mechanism of butyric acid over $Ni_{12}P_5$ cluster has been theoretically investigated at GGA-PBE/DSPP, DNP level in dodecane solution. From butyric acid, the hydrodehydration is predominated to form *n*-butanal. Then, from *n*-butanal, low temperature benefits the hydroreduction to form butanol and then hydrodehydration to produce *n*-butane, whereas high temperature favors the direct decarbonylation to yield propane. *n*-Butane originates from *n*-butanol through hydrodehydration and not from *n*-butylene. Propane comes from *n*-butanal through decarbonylation and not from propanol and/or propylene. Additionally, CO stems from *n*-butanal through decarbonylation, whereas CO_2 is ruled out from butyric acid through decarboxylation. Compared with $Ni_{12}P_6$ cluster, $Ni_{12}P_5$ cluster exhibits higher catalytic activity for the formation of butanal, *n*-butanol, and *n*-butane, while it displays lower catalytic activity toward the direct decarbonylation and dehydration to yield propylene. These results can be attributed to less negative charges of Ni-sites over $Ni_{12}P_5$ cluster, compared with $Ni_{12}P_6$ cluster.

Keywords: $Ni_{12}P_5$ cluster; deoxygenation mechanism; butyric acid; GGA-PBE; biofuel

1. Introduction

As a renewable energy, biofuel has aroused widespread concern, from the perspective of sustainable development of energy [1]. Catalytic deoxygenation of fatty acids is a promising method to produce high quality biofuel, due to the high oxygen content of fatty acids [2]. There are three deoxygenation methods, namely decarboxylation, decarbonylation and hydrodeoxygenation (HDO) [3]. Generally, there are plenty of kinds of raw materials for producing biofuel, such as palm oils and algal lipids [4,5]. Palmitic acid has commonly been preferred as a model compound of fatty acids, for the exploring the catalytic deoxygenation mechanism [6,7].

Various catalysts have been employed to produce high-quality biofuel from palmitic acid, including noble metals, base metals, and transition-metal phosphides (TMPs) [8,9]. For noble metal catalysts, they cannot be widely used because of the high cost, despite their good catalytic activity and selectivity in the deoxygenation of fatty acid [10,11]. Base metal catalysts have much lower cost than noble metal catalysts, and some of them exhibit good catalytic performance in the deoxygenation of fatty acid [12,13]. In particular, TMPs have attracted special attention, because of their activity and stability in the presence of hydrogen and oxygenated hydrocarbons, together with their cheap and accessible characteristics [14,15].

Noteworthily, nickel phosphide behaves as a promising catalyst toward the hydrodeoxygenation of palmitic acid [16,17]. Moreover, the dispersion and kinds of nickel

phosphide with the different Ni/P ratios strongly affects the deoxygenation activities and selectivities of Ni_xP catalysts [6,17]. Among them, the Ni/P molar ratios are usually be regulated by Ni_2P and/or $Ni_{12}P_5$ compounds [6,17]. One can speculate that both Ni_2P and $Ni_{12}P_5$ catalysts should exhibit different catalytic performance toward the deoxygenation of palmitic acid.

However, the current catalytic systems still face some problems, such as coke deposition, deactivation, instability, and/or large amount of hydrogen consumption [3]. These problems have urged researchers to study the selective deoxygenation mechanism of fatty acids. Encouragingly, some researchers have focused on the mechanism for the deoxygenation of different raw materials to hydrocarbon biofuels. Experimentally, Pt catalyst benefits decarboxylation [11]; MoP and Ni_2P prefer decarbonylation [14,15]; and NiMo, CoMo and WP catalyst favor hydrodeoxygenation [12,15,16]. Particularly, our group have proposed that Ni_xP facilitates both decarboxylation and decarbonylation [17], the coexistence and dispersion of both Ni_2P and $Ni_{12}P_5$ attribute the deoxygenation activity for the palmitic acid [17], and $Ni_{12}P_5$ exhibits higher turnover frequency than Ni_2P [18]. Newly, for the deoxygenation of butyric acid (as the model reactant) catalyzed by $Ni_{12}P_6$ cluster (as the Ni_2P catalyst model), decreasing temperature is favorable to the formation of butyraldehyde, *n*-butyl alcohol, and *n*-butane, and increasing temperature is beneficial to the formation of propylene, propane, and butylene [19]. Nevertheless, toward the deoxygenation of fatty acids, the molecular mechanism of $Ni_{12}P_5$ catalyst is still unclear, especially its difference in catalytic performance with Ni_2P catalyst.

In this work, comparing with Ni_2P catalyst, the deoxygenation mechanism of palmitic acid over $Ni_{12}P_5$ catalyst has been theoretically investigated. In order to improve the computational efficiency, a $Ni_{12}P_5$ cluster is constructed to model the $Ni_{12}P_5$ catalyst, with butyric acid as the reactant model. The goals are the following: (a) to obtain the elaborated potential energy curves toward the hydrodeoxygenation, decarbonylation, and decarboxylation of butyric acid over $Ni_{12}P_5$ cluster, (b) to elucidate the optimal reaction pathways for the production of propane and *n*-butane, (c) to explore the temperature effect on the rate-determining reaction step, (d) to compare the catalytic performance of $Ni_{12}P_5$ cluster with $Ni_{12}P_6$ cluster, and (f) to explore the chemical nature for the difference in catalytic performance between $Ni_{12}P_5$ cluster with $Ni_{12}P_6$ cluster, which should facilitate the rational design of highly efficient catalytic system for the deoxygenation of fatty acids.

2. Computational Methods

At the beginning, a $Ni_{12}P_5$ cluster was carved from $Ni_{12}P_5$ crystal structure in the Inorganic Crystal Structure Database (ICSD) [20], which is preferred to model $Ni_{12}P_5$-based catalyst. The dodecane (the dielectric constant is 2.016) solvent effect was taken into account by using conductor-like screening model (COSMO) [21,22], because the deoxygenation of palmitic acid has been experimentally conducted in dodecane solvent [17].

In dodecane solution, all geometry calculations were run in $Dmol^3$ module [23], using Materials Studio 7.0 package [24]. The generalized gradient approximation (GGA) and the Perdew–Burke–Ernzerhof (PBE) exchange-correlation functional were adopted [25,26]. For H, C, O, and P elements, all electrons were considered, while the core electrons were replaced by the density functional semicore pseudopotential (DSPP) for the metal Ni element [27]. The double numerical plus polarization (DNP) basis set was employed for the valence electron wave function of atoms [28], namely, GGA$-$PBE/DNP, DSPP.

The full geometry optimizations were performed for all species in the deoxygenation of butyric acid over $Ni_{12}P_5$ cluster. About the full geometric optimization, the convergence parameters were 2×10^{-3} Hartree per Å for force applied to each atom, 1.0×10^{-6} Hartree for total energy, and 5×10^{-3} Å for displacement. In addition, to improve the computational efficiency, a fermi smearing of 0.005 Hartree for orbital occupancy and a global orbital cutoff of 4.5 Å were used. The vibrational frequencies were calculated to confirm each stable intermediate or transition state, which have real frequencies for each intermediate and only one imaginary frequency for each transition state with the right

vibration direction from reactant to product. These calculation parameters are identical to those in the deoxygenation mechanism of butyric acid over $Ni_{12}P_6$ cluster [19].

The established model of $Ni_{12}P_5$ cluster is shown in Figure 1. Unless additionally noted, the Gibbs free energies of species are relative to the original $Ni_{12}P_5$ cluster and reactants (butyric acid and H_2) in dodecane solution at GGA−PBE/DSPP, DNP level, under the experimental temperature of 513.0 K [16].
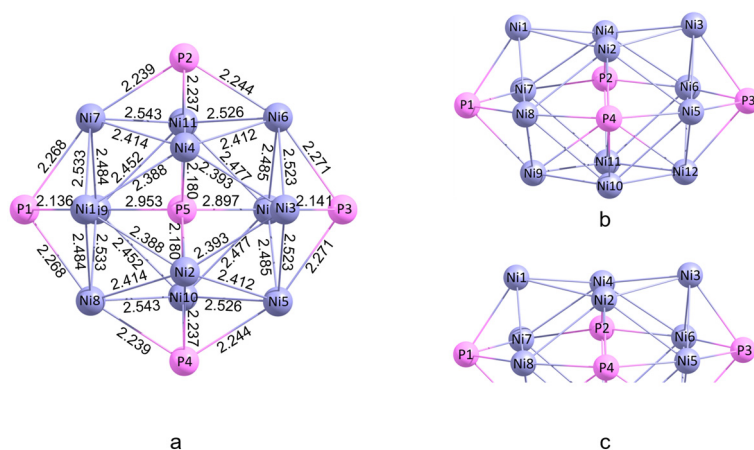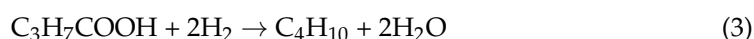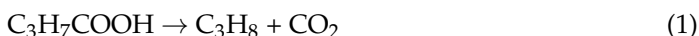

Figure 1. $Ni_{12}P_5$ cluster model, pink and purple balls represent P and Ni atoms, respectively. (**a**) Top view; (**b**) side view; and (**c**) for brevity, the atoms out of the reaction site are not shown.

For the entire catalytic cycle, the energetic span was employed to obtain both determining intermediate (DI) and determining transition state (DTS) of turnover frequency [29–34]. After that, as reported in our previous study [35], the rate constants were computed over the 413~613 K temperature range [19], based on the conventional transition state theory with tunneling correction.

3. Results and Discussion

Based on the literatures [7,19], there are three overall reactions (Reactions 1~3) for the deoxygenation of butyric acid, i.e.,

$$C_3H_7COOH \rightarrow C_3H_8 + CO_2 \tag{1}$$

$$C_3H_7COOH + H_2 \rightarrow C_3H_8 + CO + H_2O \tag{2}$$

$$C_3H_7COOH + 2H_2 \rightarrow C_4H_{10} + 2H_2O \tag{3}$$

As shown in Scheme 1, Reaction 1 is related to the direct decarboxylation of butyric acid to propane, for which there is only one reaction pathway (P-CO$_2$) with only one reaction stage (S2). Reaction 2 is associated with both decarbonylation and dehydration of butyric acid with H_2 to propane, for which there are four reaction pathways, i.e., through butanal (P-CO-nal) with two reaction stages (S3 + S4), through propanol, but not through propylene (P-CO-nol) with two reaction stages (S5 + S6), through both propanol and propylene (P-CO-nol-ene) with three reaction stages (S5 + S7a + S7b), through propylene but not through propanol (P-CO-ene) with two reaction stages (S(5/7a) + S7b). Reaction 3 is concerned with the hydrodehydration of butyric acid to *n*-butane, for which there are two reaction pathways, i.e., not through butylene (P-C4-non-ene) with three reaction stages (S3 + S8 + S9), and through butylene (P-C4-ene) with four reaction stages (S3 + F8 + F10a + F10b).

3.1. $C_3H_7COOH \rightarrow C_3H_8 + CO_2$

The potential energy curves and geometric structures for Reaction 1 of $C_3H_7COOH \rightarrow C_3H_8 + CO_2$ over $Ni_{12}P_5$ cluster are shown in Figure 2, the detailed energy data are shown in Table S1.
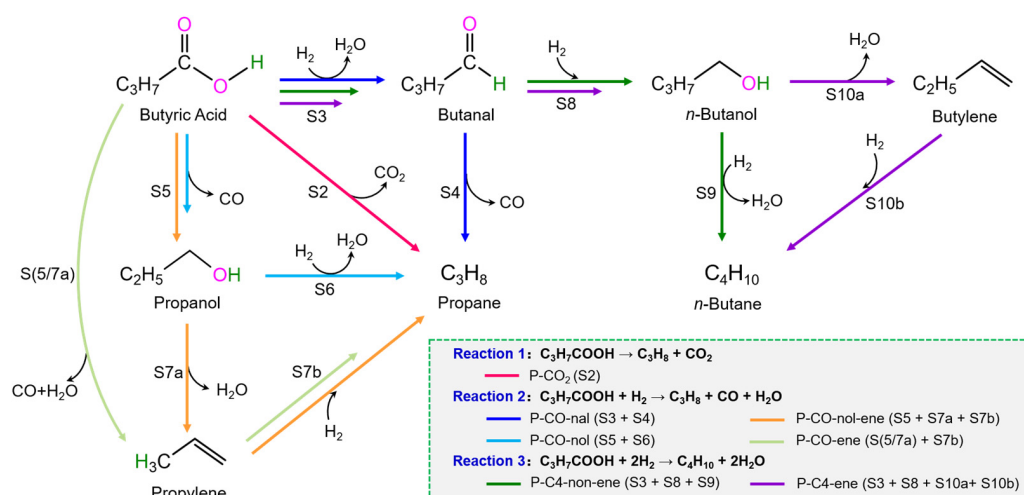
Scheme 1. Deoxygenation pathways of butyric acid over $Ni_{12}P_5$ cluster.
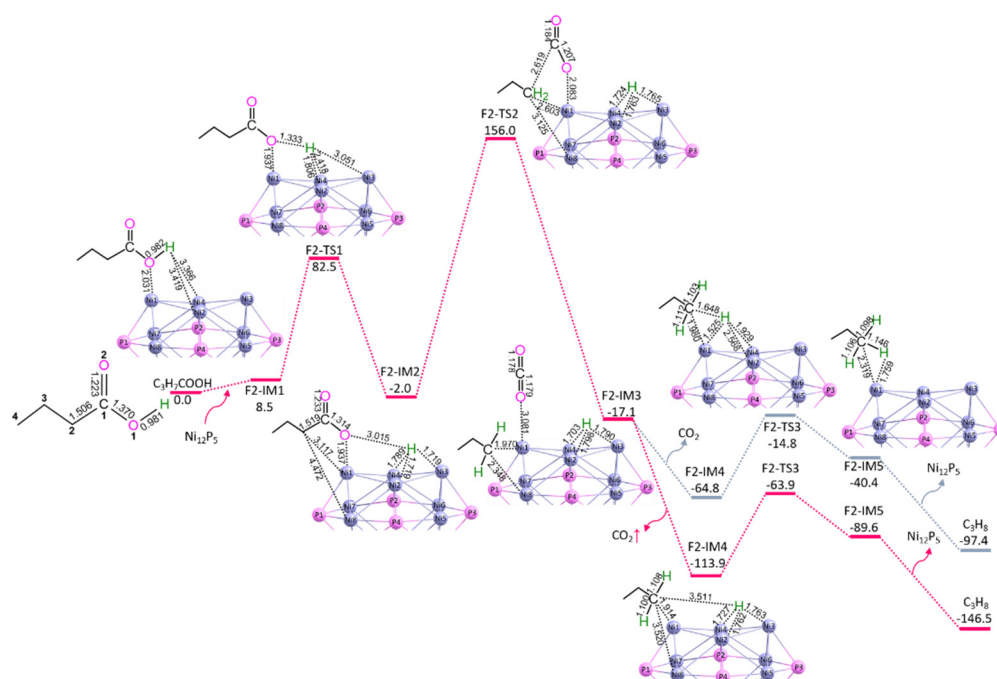
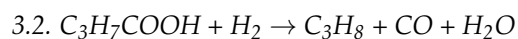

Figure 2. The potential energy curves with the relative Gibbs free energy (G_r, kJ mol^{-1}) and the geometric structures with bond lengths (Å) for reaction stage S2 over $Ni_{12}P_5$ cluster at GGA−PBE/DSPP, DNP level. For brevity, some hydrogen atoms are hidden. $CO_2\uparrow$ shows the CO_2 pressure with 10^{-5} atm under experimental condition.

As shown in Figure 2, Reaction 1 includes only one reaction pathway P-CO_2 with only one reaction stage S2. S2 is associated with the direct decarboxylation of butyric acid to propane. It mainly involves three reaction steps, i.e., (1) the cleavage of O–H bond via F2-TS1, (2) the cleavage of C1–C2 bond via F2-TS2, and (3) the formation of C2–H bond via F2-TS3.
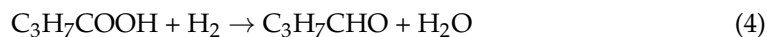
The P-CO_2 comprises the energy height of the highest point (EHHP) of 156.0 kJ mol^{-1} at F2-TS2, and the highest energy barrier (HEB) of 158.0 kJ mol^{-1} at the reaction step of F2-IM2 → F2-TS2 → F2-IM3 for the cleavage of C1–C2 bond.

3.2. $C_3H_7COOH + H_2 \rightarrow C_3H_8 + CO + H_2O$

3.2.1. P-CO-nal (S3 + S4)

As shown in Scheme 1, P-CO-nal contains two reaction stages, i.e.,

$$C_3H_7COOH + H_2 \rightarrow C_3H_7CHO + H_2O \tag{4}$$

$$C_3H_7CHO \rightarrow C_3H_8 + CO \tag{5}$$

Here, S3 (Equation (4)) and S4 (Equation (5)) are related to the hydrodehydration of butyric acid to butanal, and the decarbonylation of butanal to propane, respectively. The potential energy curves and geometric structures for reaction stages of S3 and S4 over $Ni_{12}P_5$ cluster are depicted in Figures 3 and 4, respectively. The detailed energy data are shown in Tables S2 and S3.
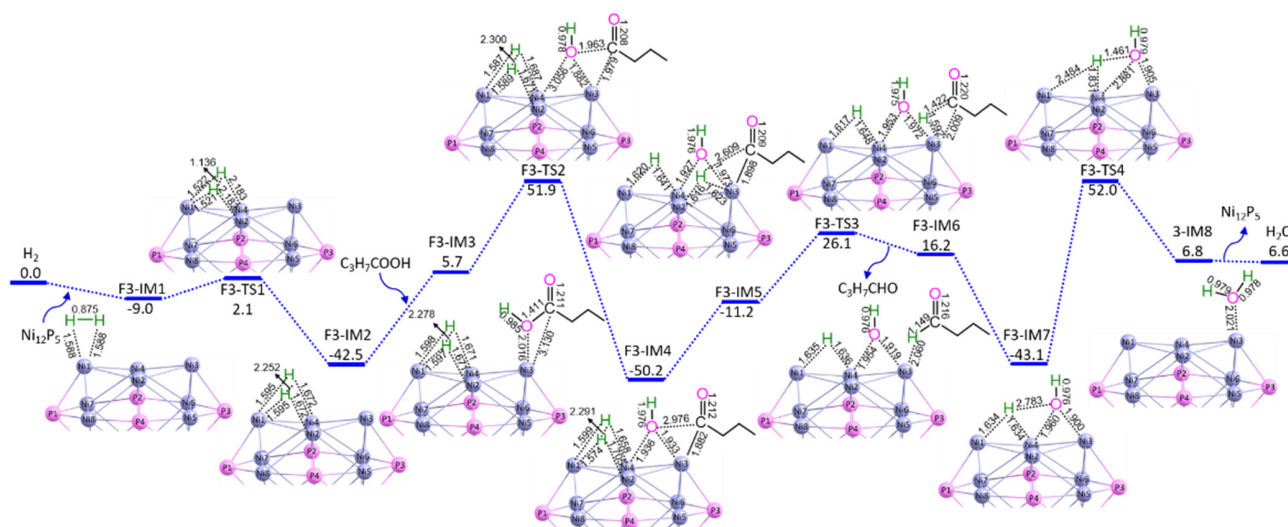
Figure 3. The potential energy curves with the relative Gibbs free energy (G_r, kJ mol^{-1}) and the geometric structures with bond lengths (Å) for reaction stage S3 over $Ni_{12}P_5$ cluster at GGA−PBE/DSPP, DNP level. For brevity, some hydrogen atoms are hidden.
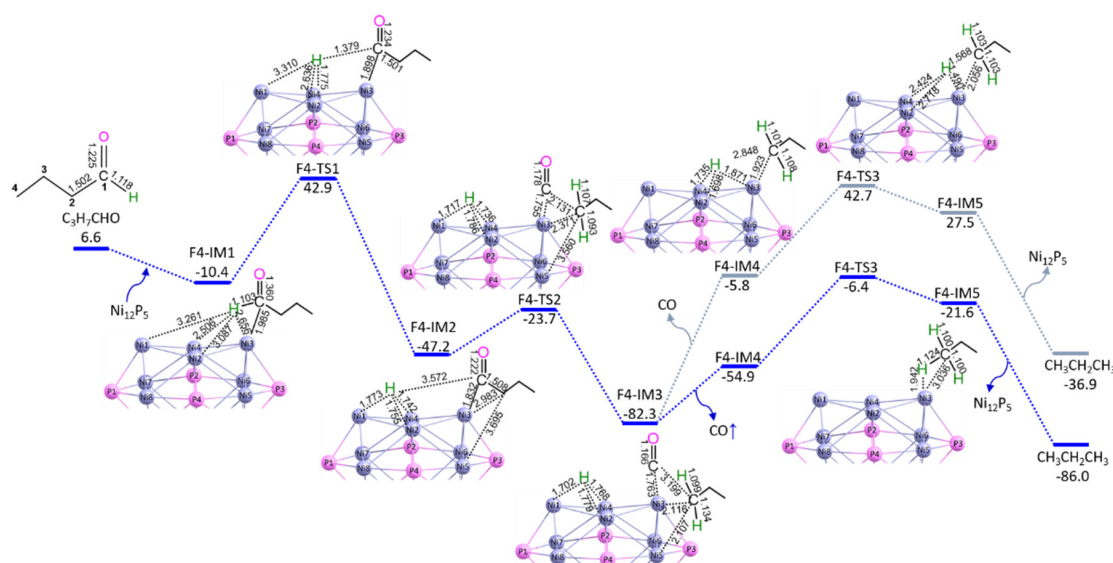
Figure 4. The potential energy curves with the relative Gibbs free energy (G_r, kJ mol^{-1}) and the geometric structures with bond lengths (Å) for reaction stage S4 over $Ni_{12}P_5$ cluster at GGA−PBE/DSPP, DNP level. For brevity, some hydrogen atoms are hidden. CO↑ shows the CO pressure with 10^{-5} atm under experimental condition.

As shown in Figure 3, S3 mainly contains four reaction steps, i.e., (1) the dissociation of H_2 via F3-TS1, (2) the cleavage of C1–OH bond via F3-TS2, (3) the formation of C1–H bond via F3-TS3, and (4) the formation of HO–H bond via F3-TS4.

Moreover, as depicted in Figure 4, S4 mainly involves three sequential reaction steps, i.e., (1) the cleavage of C1–H bond via 4-TS1, (2) the cleavage of C1–C2 bond via F4-TS2, and (3) the formation of C2–H bond via five-membered F4-TS3.

The P-CO-nal with S3 and S4 includes the EHHP of 52.0 kJ mol^{-1} at F3-TS4, and the HEB of 95.1 kJ mol^{-1} at F3-IM7 → F3-TS4 → F3-IM8 reaction step for the HO–H bond formation.

3.2.2. P-CO-nol (S5 + S6)

As shown in Scheme 1, P-CO-hol contains two reaction stages, i.e.,

$$C_3H_7COOH \rightarrow C_3H_7OH + CO \tag{6}$$

$$C_3H_7OH + H_2 \rightarrow C_3H_8 + H_2O \tag{7}$$
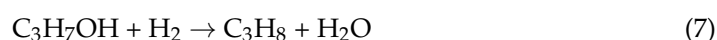
Here, S5 (Equation (6)) and S6 (Equation (7)) are related to the direct decarbonylation of butyric acid to propanol, and the hydrodehydration of propanol to propane, respectively. The potential energy curves and geometric structures for reaction stages of S5 and S6 over $Ni_{12}P_5$ cluster are shown in Figures 5 and 6, respectively. The detailed energy data are shown in Tables S4 and S5.
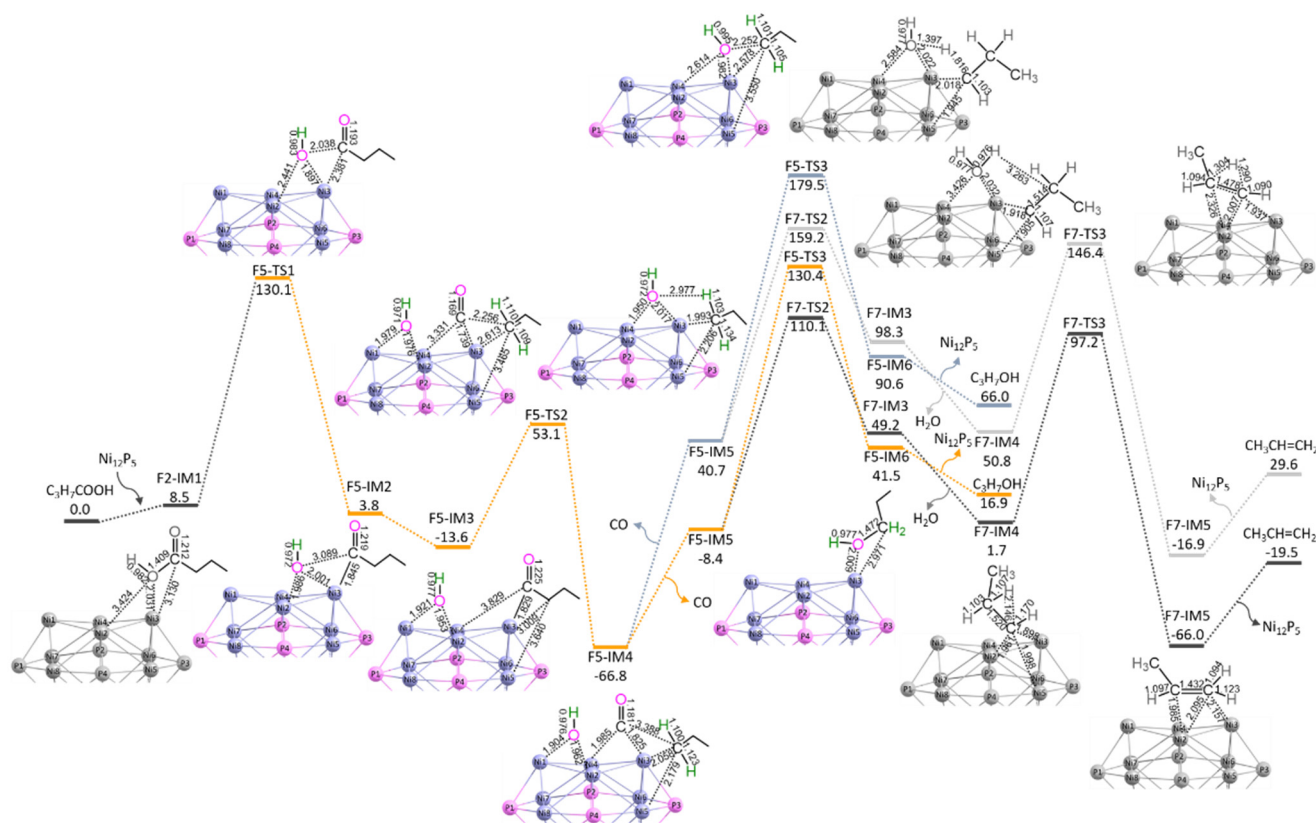
Figure 5. The potential energy curves with the relative Gibbs free energy (G_r, kJ mol^{-1}) and the geometric structures with bond lengths (Å) for reaction stages S5 (the yellow line) and S5/7a (the black line) over $Ni_{12}P_5$ cluster at GGA−PBE/DSPP, DNP level. For brevity, some hydrogen atoms are hidden. CO↑ shows the CO pressure with 10^{-5} atm under experimental condition.
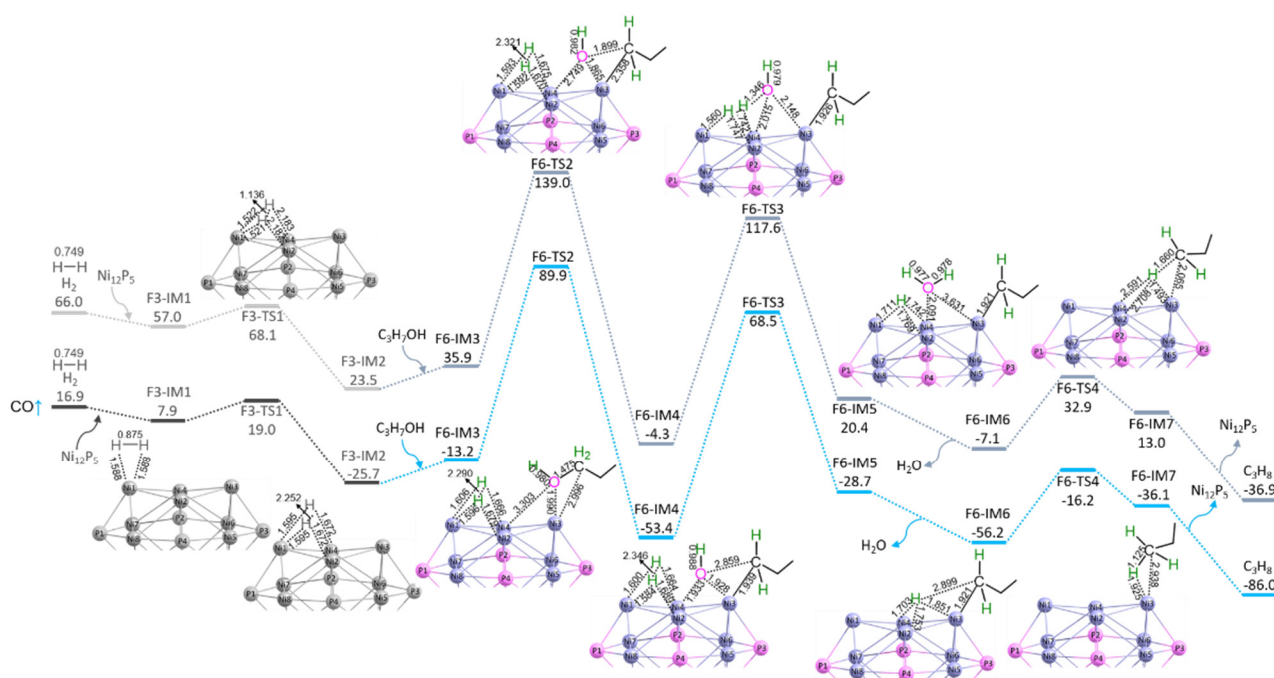
Figure 6. The potential energy curves with the relative Gibbs free energy (G_r, kJ mol^{-1}) and the geometric structures with bond lengths (Å) for reaction stage S6 over Ni$_{12}$P$_5$ cluster at GGA−PBE/DSPP, DNP level. For brevity, some hydrogen atoms are hidden. CO↑ shows the CO pressure with 10^{-5} atm under experimental condition.

As depicted in Figure 5, S5 mainly contains three reaction steps, i.e., (1) the cleavage of C1–OH bond via 5-TS1, (2) the cleavage of C1–C2 bond via F5-TS2, and (3) the formation C2–OH bond via F5-TS3.

Additionally, as shown in Figure 6, S6 mainly includes four reaction steps, i.e., (1) the dissociation of H$_2$ via F3-TS1, (2) the cleavage of C2–OH bond via F6-TS2, (3) HO–H bond formation via F6-TS3, and (4) C2–H bond formation via F6-TS4.

The P-CO-hol with S5 and S6 comprises the EHHP of 130.4 kJ mol^{-1} at F5-TS3, and the HEB of 138.8 kJ mol^{-1} at F5-IM5 → F5-TS3 → F5-IM5 reaction step for the formation of C2–OH bond.

3.2.3. P-CO-nol-ene (S5 + S7a + S7b)

As shown in Scheme 1, the P-CO-nol-ene consists of three reaction stages, i.e., S5, S7a (Equation (8)) and S7b (Equation (9)),

$$C_3H_7OH \rightarrow C_3H_6 + H_2O \tag{8}$$

$$C_3H_6 + H_2 \rightarrow C_3H_8 \tag{9}$$

As mentioned earlier, S5 is typical of the direct decarbonylation of butyric acid to propanol. Here, S7a and S7b are related to the dehydration of propanol to propylene and hydrogenation of propylene to propane, respectively. The potential energy curves and geometric structures for S7a and S7b over Ni$_{12}$P$_5$ cluster are depicted in Figure 7, respectively. The detailed energy data are shown in Tables S6 and S7.

As shown in Figure 7a, S7a mainly involves three reaction steps, i.e., (1) the cleavage of C2–OH bond via F7-TS1, (2) both the cleavage of C2–H bond and the formation of HO–H bond via F7-TS2, and (3) intramolecular [1,2]-H shift via F7-TS3.

As shown in Figure 7b, S7b mainly contains three reaction steps, i.e., (1) the dissociation of H$_2$ via F3-TS1, (2) the formation of C3–H bond via F7-TS4, (3) the formation of C2–H bond via F7-TS5.

The P-CO-nol-ene with S5, S7a and S7b comprises the EHHP of 130.4 kJ mol^{-1} at F5-TS3, and the HEB of 138.8 kJ mol^{-1} at F5-IM5 → F5-TS3 → F5-IM5 reaction step for the formation of C2–OH bond.


(a)

(b)
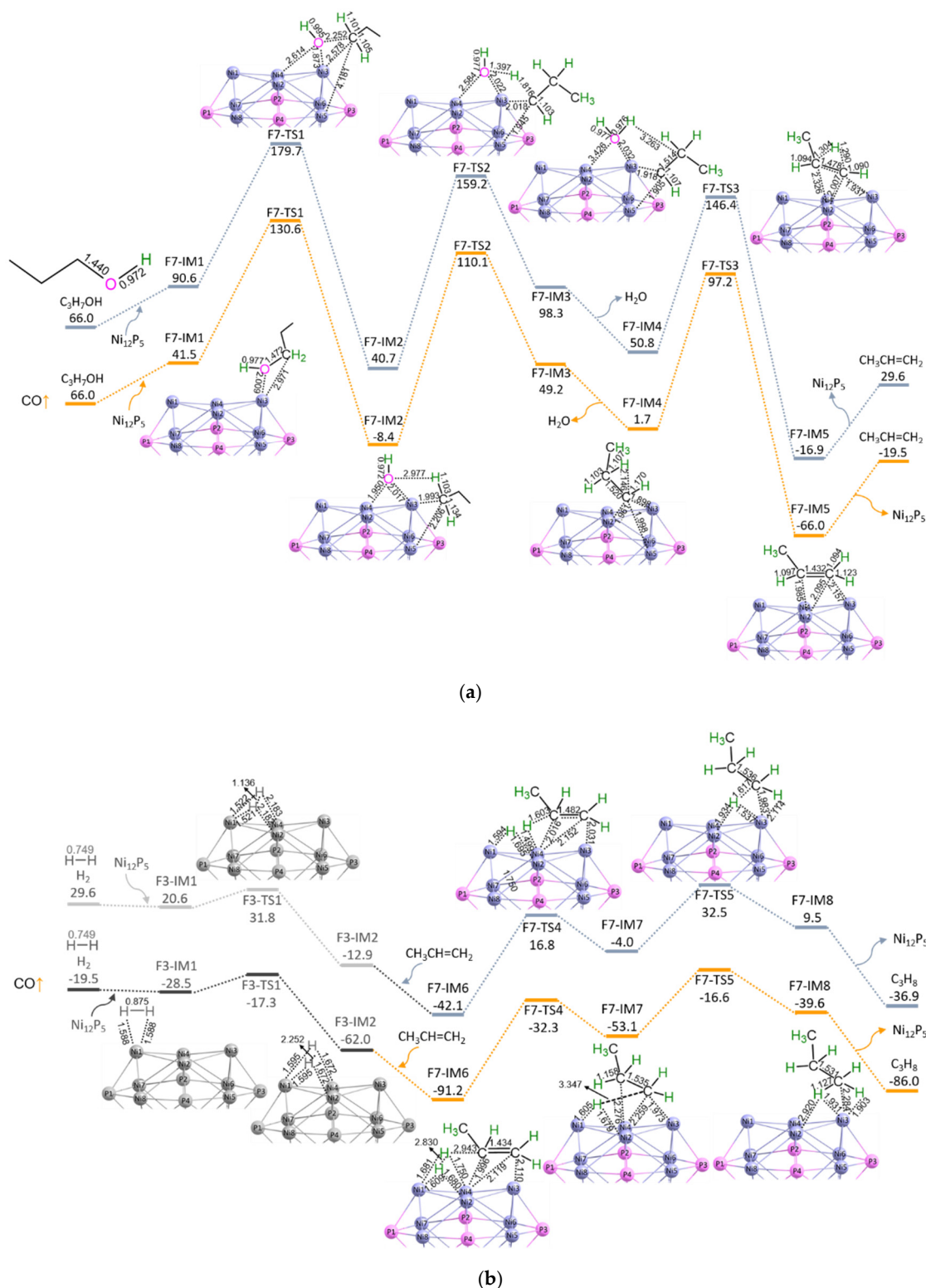
Figure 7. The potential energy curves with the relative Gibbs free energy (G_r, kJ mol^{-1}) and the geometric structures with bond lengths (Å) for reaction stages S7a (**a**) and S7b (**b**) over Ni$_{12}$P$_5$ cluster at GGA−PBE/DSPP, DNP level. For brevity, some hydrogen atoms are hidden. CO↑ shows the CO pressure with 10^{-5} atm under experimental condition.

3.2.4. P-CO-ene (S5/7a + S7b)

As shown in Scheme 1, the P-CO-ene is composed of two reaction stages, i.e., S(5/7a) (Equation (10)) and S7b,

$$C_3H_7COOH \rightarrow C_3H_6 + CO + H_2O \tag{10}$$
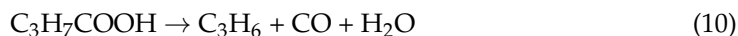
Here, S(5/7a) is concerned with the direct dehydration and decarbonylation of butyric acid to propylene. As mentioned earlier, S7b is associated with hydrogenation of propylene to propane. Furthermore, S(5/7a) can be composed S5 and S7a, but without propanol. The potential energy curves and geometric structures the for S(5/7a) over $Ni_{12}P_5$ cluster are shown in Figure 5. As mentioned earlier, S7b is the hydrogenation of propylene to propane.

As depicted in Figure 5, S(5/7a) mainly consists of four reaction steps, i.e., (1) the cleavage of C1–OH bond via F5-TS1, (2) the cleavage of C1–C2 bond via F5-TS2, (3) the cleavage of C2–H bond and the formation of HO–H bond via F7-TS2, and (4) intramolecular [1,2]-H shift via F7-TS3.
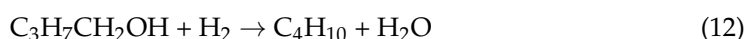
The P-CO-ene with S(5/7a) and S7b includes the EHHP of 130.1 kJ mol^{-1} at F5-TS1, and the HEB of 121.6 kJ mol^{-1} at F2-IM1 → F5-TS1 → F5-IM2 reaction step for the cleavage of C1–OH bond.

Summarily, for Reaction 2, P-CO-nal is kinetically more favorable than P-CO-nol, P-CO-nol-ene, and P-CO-ene, owing to their lower EHHPs (52.0 vs. 130.4, 130.4, and 130.1 kJ mol^{-1}) and lower HEBs (95.1 vs. 138.8, 138.8, and 121.6 kJ mol^{-1}). In other words, P-CO-nal should be the optimal pathway for Reaction 2, which proceeds through sequential hydrodehydration and decarbonylation via butanal intermediate, whereas it does not accompany both propanol and propylene intermediates. This result is analogous to the experimental phenomena for the deoxygenation of palmitic acid over $Ni_{12}P_5$-based catalyst, in which both pentadecanol and pentadecene were not observed [18].
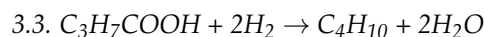
3.3. $C_3H_7COOH + 2H_2 \rightarrow C_4H_{10} + 2H_2O$
3.3.1. P-C4-non-ene (S3 + S8 + S9)

As shown in Scheme 1, the P-C4-non-ene comprises three reaction stages, i.e., S3, S8 (Equation (11)), and S9 (Equation (12)),

$$C_3H_7CHO + H_2 \rightarrow C_3H_7CH_2OH + H_2O \tag{11}$$

$$C_3H_7CH_2OH + H_2 \rightarrow C_4H_{10} + H_2O \tag{12}$$

As mentioned earlier, S3 is typical of the hydrodehydration of butyric acid to butanal. Here, S8 is related to the hydroreduction of butanal to *n*-butanol, and S9 is concerned with the hydrodehydration of *n*-butanol to *n*-butane. The potential energy curves and geometric structures for S8 and S9 over $Ni_{12}P_5$ cluster are shown in Figures 8 and 9, respectively. The detailed energy data are shown in Tables S8 and S9.

As shown in Figure 8, S8 mainly contains three reaction steps, i.e., (1) the dissociation of H_2 via F3-TS1, (2) the formation of O–H bond via F8-TS2, and (3) the formation of C1–H bond via F8-TS3.

In addition, as depicted in Figure 9, S9 mainly consists of four reaction steps, i.e., (1) the dissociation of H_2 via F3-TS1, (2) the cleavage of C1–OH bond via F9-TS2, (3) the formation of HO–H bond via F9-TS3, and (4) C1–H bond formation via F9-TS4.

The P-C4-non-ene with S3, S8, and S9 involves the EHHP of 84.9 kJmol^{-1} at F8-TS3 for the formation of C1–H bond, and the HEB of 115.2 kJmol^{-1} at F9-IM3 → F9-TS2 → F9-IM4 reaction step for the cleavage of C1–OH bond.
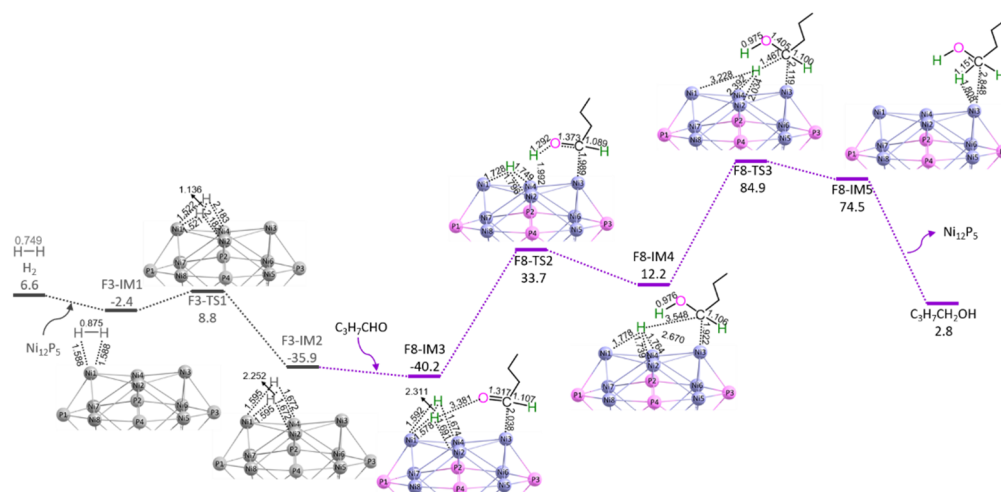
Figure 8. The potential energy curves with the relative Gibbs free energy (G_r, kJ mol^{-1}) and the geometric structures with bond lengths (Å) for reaction stage S8 over Ni$_{12}$P$_5$ cluster at GGA−PBE/DSPP, DNP level. For brevity, some hydrogen atoms are hidden.
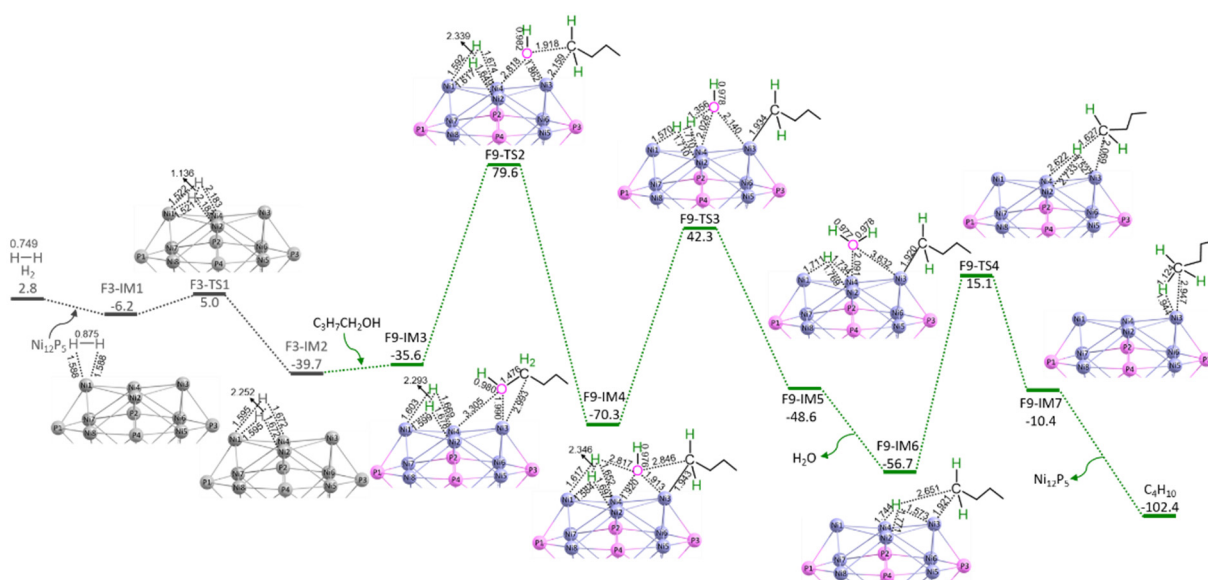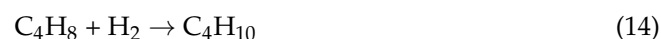

Figure 9. The potential energy curves with the relative Gibbs free energy (G_r, kJ mol^{-1}) and the geometric structures with bond lengths (Å) reaction stage S9 over Ni$_{12}$P$_5$ cluster at GGA−PBE/DSPP, DNP level. For brevity, some hydrogen atoms are hidden.

3.3.2. P-C4-ene (S3 + S8 + S10a + S10b)

As depicted in Scheme 1, the P-C4-ene consists of four reaction stages, i.e., S3, S8, S10a (Equation (13)), and S10b (Equation (14)),

$$C_3H_7CH_2OH \rightarrow C_4H_8 + H_2O \tag{13}$$

$$C_4H_8 + H_2 \rightarrow C_4H_{10} \tag{14}$$

As mentioned earlier, S3 and S8 are typical of the hydrodehydration of butyric acid to butanal and the hydroreduction of butanal to *n*-butanol, respectively. Here, both S10a and S10b are related to the dehydration of *n*-butanol to butylene and hydrogenation of butylene to *n*-buane, respectively. The potential energy curves and geometric structures for S10a and S10b over Ni$_{12}$P$_5$ cluster are depicted in Figure 10. The detailed energy data are shown in Tables S10 and S11.
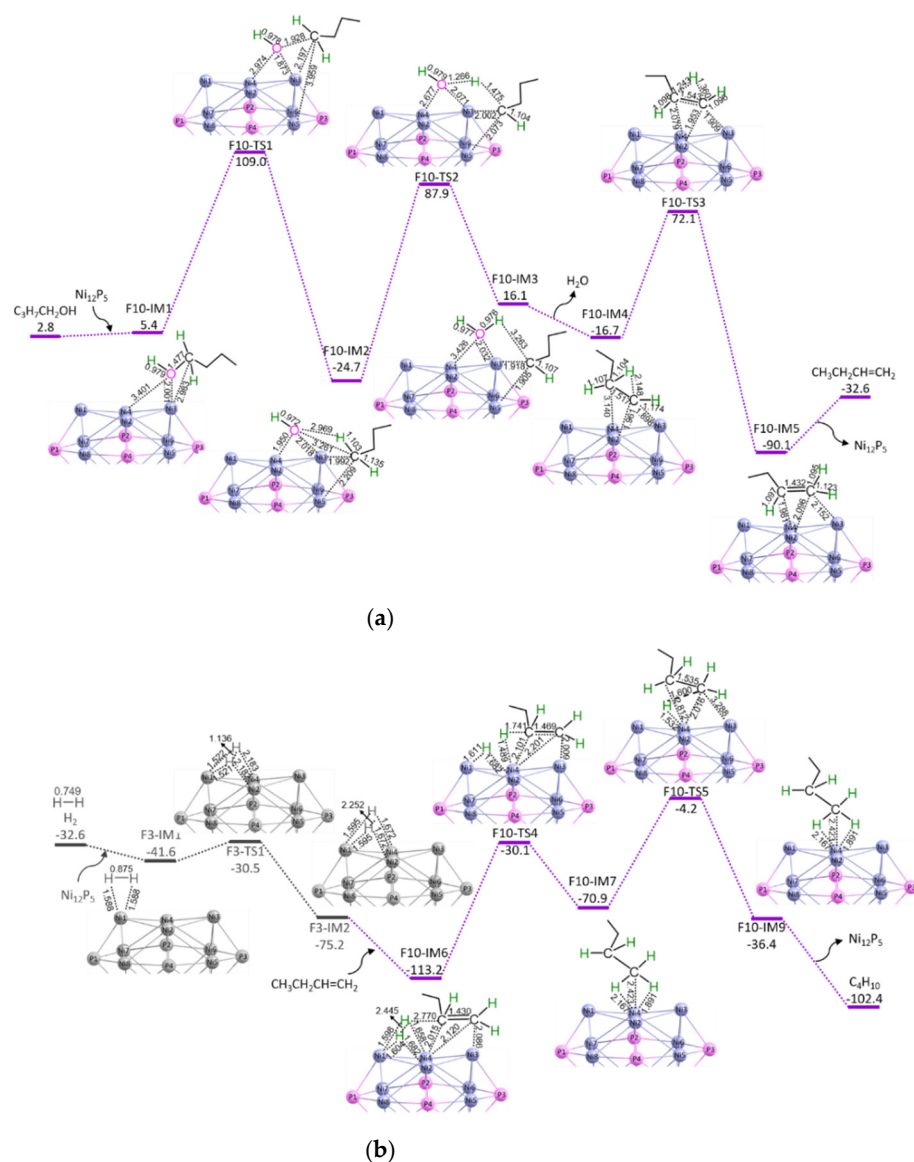
Figure 10. The potential energy curves with the relative Gibbs free energy (G_r, kJ mol^{-1}) and the geometric structures with bond lengths (Å) reaction stages S10a (**a**) and S10b (**b**) over Ni$_{12}$P$_5$ cluster at GGA−PBE/DSPP, DNP level. For brevity, some hydrogen atoms are hidden.

As shown in Figure 10a, S10a mainly includes three reaction steps, i.e., (1) the cleavage of C1–OH bond via F10-TS1, (2) both the cleavage of C2–H bond and the formation of HO–H bond via F10-TS2, and (3) intramolecular H-shift via F10-TS3.

In addition, as depicted in Figure 10b, S10b mainly contains three reaction steps, i.e., (1) the dissociation of H$_2$ via F3-TS1, (2) the formation of C2–H bond via F10-TS4, and (3) the cleavage of C1–H bond via F10-TS5.

The P-C4-ene with S3, S8, S10a, and S10b comprises the EHHP of 109.0 kJmol^{-1} at F10-TS1 for the C1–OH bond cleavage, and the HEB of 112.6 kJmol^{-1} at F10-IM2 → F10-TS2 → F10-IM3 reaction step for both the cleavage of C2–H bond and the formation of HO–H bond.

In brief, for Reaction 3, P-C4-non-ene is preferable to P-C4-ene in kinetics, owing to its lower EHHP (84.9 vs. 109.0 kJ mol^{-1}) and similar HEB (115.2 vs. 112.6 kJ mol^{-1}). In other words, P-C4-non-ene is the optimal reaction pathway for Reaction 3, which goes through both butanal and *n*-butanol, and without through butylene. This result is similar to the experimental result, in which hexadecanol was observed without observation of hexadecene for the hydrodeoxygenation of palmitic acid over Ni$_{12}$P$_5$-based catalyst [18].

3.4. Catalytic Selectivity Dependent on Temperature

3.4.1. From Butyric Acid

As shown in Scheme 1, from butyric acid, there are four competitive reaction stages, i.e., S2, S3, and S5, and S(5/7a). In view of S2, the DTS and DI are ascertained to be F2-TS2 and F2-IM2, respectively. As shown in Figure S1, The formula of the rate constant for S2 (k_{S2}) can be fitted as follows (15, in s^{-1}):

$$k_{S2} = 2.88 \times 10^{14} \exp(-172\,166/RT) \tag{15}$$

As to S3, the DTS and DI are determined to be (F3-TS4 + butanal) and F3-IM4, respectively. As shown in Figure S2, the formula of the rate constant for S3 (k_{S3}) can be expressed as follows (16, in s^{-1}):

$$k_{S3} = 1.79 \times 10^{20} \exp(-174\,054/RT) \tag{16}$$

Taking S5 into accounts, the DTS and DI are computed to be (F5-TS3 + CO) and F5-IM4, respectively. As shown in Figure S4, the formula of the rate constant for S5 (k_{S5}) can be adapted as follows (17, in s^{-1}):

$$k_{S5} = 1.23 \times 10^{21} \exp(-327\,015/RT) \tag{17}$$

Considering S(5/7a), the DTS and DI are ascertained to be (F7-TS2 + CO) and F5-IM4, respectively. As shown in Figure S5, the formula of the rate constant for S(5/7a) ($k_{S(5/7a)}$) can be represented as follows (18, in s^{-1}):

$$k_{S(5/7a)} = 4.45 \times 10^{21} \exp(-306\,230/RT) \tag{18}$$

From the formulas i~iv, the selectivity of S3 is 100%, while the total selectivity of S2, S5, and S(5/7a) is nearly to zero, over the 413~613 K temperature range. As a result, S3 is predominated while S2, S5, and S(5/7a) should be ruled out. That is to say, both direct decarboxylation and direct decarbonylation should not be possible reaction pathway for the deoxygenation of butyric acid over $Ni_{12}P_5$ cluster. This result is analogous to the experimental result, in which CO_2 was not observed during the hydrodeoxygenation of palmitic acid over $Ni_{12}P_5$-based catalyst [18].

3.4.2. From Butanal

As shown in Scheme 1, from butanal, there are two competitive reaction stages, i.e., S4 and S8, which result in the formation of (C_3H_8 + CO) and $C_3H_7CH_2OH$, respectively. For S4, the DTS and DI are computed to be (F4-TS3 + CO) and F4-IM3, respectively. As shown in Figure S3, the formula of the rate constant for S4 (k_{S4}) can be expressed as follows (19, in s^{-1}):

$$k_{S4} = 3.65 \times 10^{18} \exp(-175\,375/RT) \tag{19}$$

Additionally, for S8, the DTS and DI are calculated to be F8-TS3 and F8-IM3, respectively. As shown in Figure S6, the formula of the rate constant for S8 (k_{S8}) can be described as follows (20, in s^{-1}):

$$k_{S8} = 1.00 \times 10^{12} \exp(-95\,469/RT) \tag{20}$$

In view of k_{S4} and k_{S8}, their selectivities are 0.3~85.0% and 99.7~15.0%, respectively, over the 413~613 K temperature range. Among them, their selectivities are equal to 50.0% at about 553 K. It is inferred that S8 for the hydrogenation to *n*-butanol is governed at low temperature (413~553 K), whereas S4 for the decarbonylation to propane is dominated at high temperature (553~613 K). In other words, decreasing the temperature is advantageous to hydrogenation to *n*-butanol, and increasing the temperature is beneficial to the decarbonylation to propane.

3.4.3. From n-Butanol

As shown in Scheme 1, from *n*-butanol, there are two competitive reaction pathways, i.e., S9 and S10, which lead to the synergistic hydrodehyration to *n*-butane and the stepwise dehydration and hydrogenation to *n*-butane via butylene intermediate, respectively. For S9, the DTS and DI are ascertained to be F9-TS2 and F9-IM3, respectively. As shown in Figure S7, the formula of the rate constant for S9 (k_{S9}) can be adapted as follows (21, in s^{-1}):

$$k_{S9} = 4.32 \times 10^{11} \exp(-100\,816/RT) \tag{21}$$

Alternatively, for S10, the DTS and DI are to determined be F10-TS1 and (F10-IM5 + H_2O), respectively, in which the DTS (F10-TS1) lies before the DI (F10-IM5 + H_2O). As shown in Figure S8, the formula of the rate constant for S10 (k_{S10}) can be fitted as follows (22, in s^{-1}):

$$k_{S10} = 1.55 \times 10^{12} \exp(-156\,411/RT) \tag{22}$$

In view of both k_{S9} and k_{S10a}, the selectivity of S9 is 100%, while the selectivity of S10 is close to zero, over the 413~613 K temperature range. It is indicated that *n*-butane stems from S9 (synergistic hydrodehydration), and it goes not through butylene.

As mentioned earlier, for the deoxygenation of butyric acid over $Ni_{12}P_5$ cluster, there are two kinds of alkanes, i.e., propane and *n*-butane. On the one hand, for the propane formation, the DTS and DI are computed to be (F3-TS4 + C_3H_7CHO) and F3-IM4, respectively, on the optimal reaction pathway P-CO-nal. Thereupon, for the propane formation, the corresponding rate constants of $k_{C_3H_8}$ (23, in s^{-1}) are identical to k_{S3}, i.e.,

$$k_{C_3H_8} = 1.79 \times 10^{20} \exp(-174\,054/RT) \tag{23}$$

On the other hand, for the *n*-butane formation, the DTS and DI are calculated to be (F8-TS3 + H_2O) and (F3-IM4 + H_2), respectively, on the optimal reaction pathway P-C4-non-ene. As shown in Figure S9, the rate constant $k_{C_4H_{10}}$ can be fitted as follows (24, in $s^{-1}\,mol^{-1}\,dm^3$):

$$k_{C_4H_{10}} = 6.26 \times 10^{11} \exp(-103\,468/RT) \tag{24}$$

Based on the rate constants of $k_{C_3H_8}$ and $k_{C_4H_{10}}$, when the concentration of H_2 is the standard concentration of 1.0 mol dm^{-3}, the selectivity of C_3H_8 is calculated to be 25.2~99.6%, while the selectivity of C_4H_{10} is computed to be 74.8~0.4%, over the temperature range of 413~613 K. Generally, in the experimental temperature range (513~553 K) [7,18], the selectivities of C_3H_8 and C_4H_{10} are 94.9~98.4% and 5.1~1.6%, respectively. That is to say, at the normal experimental temperature, the selectivity of C_3H_8 is higher than that of C_4H_{10}. This result is qualitatively in agreement with the experimental result with 59.8% yield for C15 and 33.7% yield for C16 for the hydrodeoxygenation of palmitic acid over $Ni_{12}P_5$-based catalyst [18].

In short, there exist two main reactions for the deoxygenation of butyric acid over $Ni_{12}P_5$ cluster, i.e., Reaction 2 for the propane formation and Reaction 3 for the *n*-butane formation, while Reaction 1 for the decarboxylation should be ruled out. Herein, propane comes from P-CO-nal with S3 and S4 via butanal intermediate in Reaction 2. *n*-Butane stems from P-C4-non-ene with S3, S8 and S9 via both butanal and *n*-butanol intermediates and not via butylene in Reaction 3. From the crucial butanal intermediate, decreasing the temperature is favorable to the hydrodehydration to *n*-butane, and increasing the temperature is preferable to the decarbonylation to propane. The dominant reaction pathways with the temperature effect for the hydrodeoxygenation of butyric acid over $Ni_{12}P_5$ cluster are shown in Figure 11.
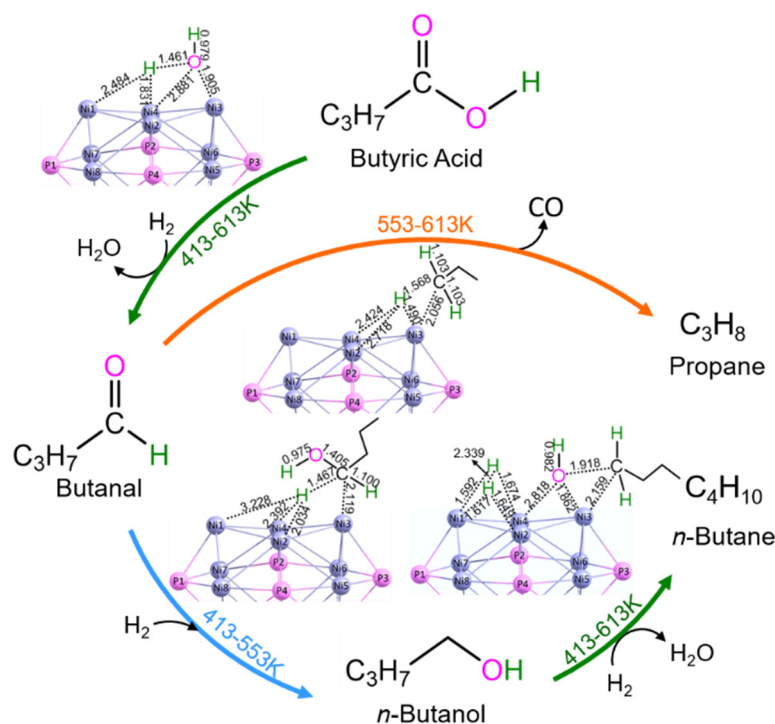
Figure 11. The main reaction pathways for the deoxygenation of butyric acid over $Ni_{12}P_5$ cluster.

### 3.5. Comparison of $Ni_{12}P_5$ Cluster with $Ni_{12}P_6$ Cluster in the Catalytic Performance

As discussed above, for the C_4H_{10} formation in Reaction 3, on the optimal reaction pathway, the rate constants of k_{C4H10} over $Ni_{12}P_5$ cluster are calculated to be 2~3 order of magnitude larger than that over $Ni_{12}P_6$ cluster [19], if the concentration of each reactant is the standard concentration of 1.0 mol dm^{-3}. Therein, over $Ni_{12}P_6$ cluster, the crucial transition state F3-TS3 is associated with the formation of C1–H bond. The energy barrier of F3-IM5 → F3-TS3 over $Ni_{12}P_5$ cluster is 37.3 kJ mol^{-1}, which is apparently lower than that (59.3 kJ mol^{-1}) over $Ni_{12}P_6$ cluster. It is inferred that $Ni_{12}P_5$ cluster exhibits better catalytic activity than $Ni_{12}P_6$ cluster toward C1–H bond formation.

For the C_3H_8 formation in Reaction 2, on the typical reaction pathway P-CO-ene, the formation rate of r_{C3H8} over $Ni_{12}P_5$ cluster are computed to be 5~2 order of magnitude smaller than that over $Ni_{12}P_6$ cluster [19], if the concentration of each reactant is the standard concentration of 1.0 mol dm^{-3}. Wherein, the C1–C2 bond cleavage is characteristic of F5-TS2. The energy barrier of F5-IM3 → F5-TS2 over $Ni_{12}P_6$ cluster is 31.0 kJ mol^{-1} [19], which is obviously lower than that (66.7 kJ mol^{-1}) over $Ni_{12}P_5$ cluster. It is indicated that $Ni_{12}P_6$ cluster displays better catalytic activity than $Ni_{12}P_5$ cluster toward C1–C2 bond cleavage.

To gain insight into the chemical nature for the difference in catalytic performance between $Ni_{12}P_5$ cluster with $Ni_{12}P_6$ cluster, the corresponding Mulliken charges for F3-TS3 and F5-TS2 over $Ni_{12}P_5$ cluster and for 3-TS3 and 5-TS2 over $Ni_{12}P_6$ cluster are analyzed in Figure 12.

As shown in Figure 12a, over $Ni_{12}P_5$ cluster, the Mulliken charges of both Ni1~Ni12 moiety and P1~P5 moiety are −2.902 and +2.902, respectively. As depicted in Figure 12b, over $Ni_{12}P_6$ cluster, the Mulliken charges of both Ni1~Ni12 moiety and P1~P6 moiety are −3.217 and +3.217, respectively. It is indicated that the charge of catalytically active Ni-site over $Ni_{12}P_5$ cluster is less negative than that over $Ni_{12}P_6$ cluster. Over both $Ni_{12}P_5$ and $Ni_{12}P_6$ clusters, the valence electrons of P atom are partly filled into the empty orbit of Ni atom, making the Ni1~Ni12 moiety negative charge. That is to say, over Ni_xP_y cluster, the more P atoms, the more negative the charge of nickel atoms.
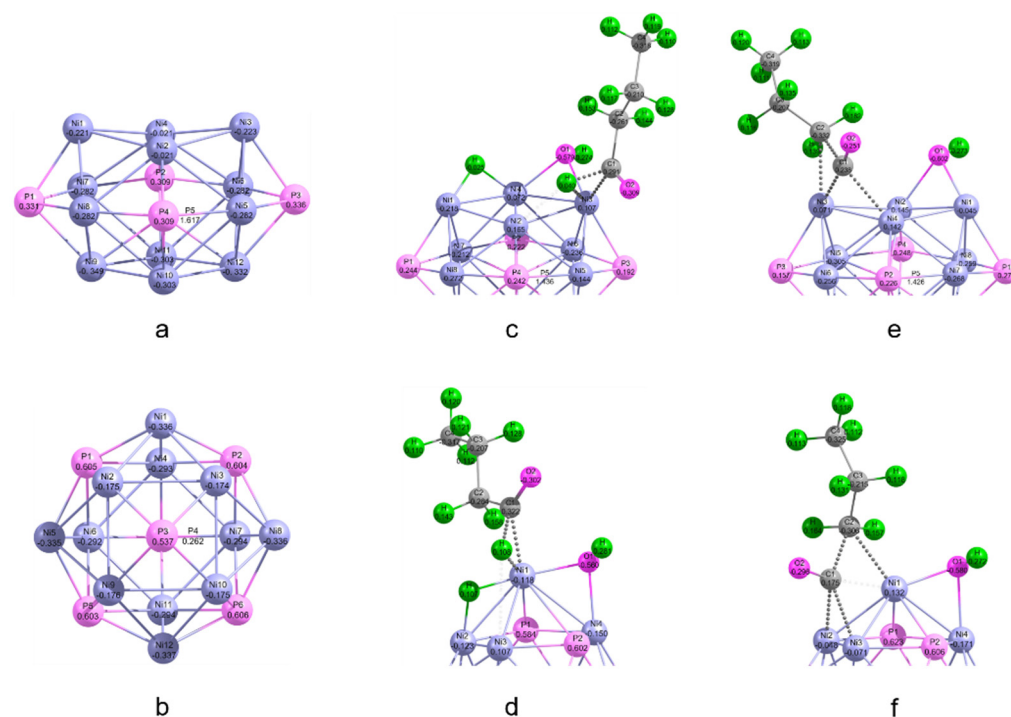
Figure 12. Mulliken charges for (**a**) $Ni_{12}P_5$ cluster, (**b**) $Ni_{12}P_6$ cluster, (**c**) F3-TS3 over $Ni_{12}P_5$ cluster, (**d**) 3-TS3 over $Ni_{12}P_6$ cluster, (**e**) F5-TS2 over $Ni_{12}P_5$ cluster, and (**f**) 5-TS2 over $Ni_{12}P_6$ cluster, respectively.

As displayed in Figure 12c,d, the charge of catalytically active Ni3-site in F3-TS3 is +0.107 over $Ni_{12}P_5$ cluster, whereas the charge of catalytically active Ni1-site in 3-TS3 is −0.118 over $Ni_{12}P_6$ cluster. Over $Ni_{12}P_5$ cluster, the Ni3–site on three-membered cyclic F3-TS3 is positive charge, which weakens the Ni3–H interaction and then induces it easy for the formation of C1–H bond. Alternatively, over $Ni_{12}P_6$ cluster, the Ni1-site on three-membered cyclic 3-TS3 is negative charge, which enhances the Ni1–H interaction and then makes it difficult for the formation of C1–H bond.

As depicted in Figure 12e,f, the charges of catalytically active Ni3- and Ni4-sites in F5-TS2 are +0.071 and +0.142 over $Ni_{12}P_5$ cluster, respectively, whereas the charge of catalytically active Ni2- and Ni3-sites in 5-TS2 are −0.048 and −0.071 over $Ni_{12}P_6$ cluster, respectively. Over $Ni_{12}P_5$ cluster, both Ni3- and Ni4-sites on four-membered cyclic F5-TS2 are positive charge, which abates the Ni3–C1 and Ni4–C1 interactions and then impels it difficult for the cleavage of C1–C2 bond. On the other hand, over $Ni_{12}P_6$ cluster, both Ni2- and Ni3-sites on five-membered 5-TS2 are negative charge, which boosts the Ni2–C1 and Ni3–C1 interactions and then causes it ready for the cleavage of C1–C2 bond.

Shortly, over Ni_xP_y cluster, the fewer the P atoms, the less negative the charge of Ni atoms, the weaker the Ni–H interaction, and the easier the formation of C–H bond. Alternatively, the greater the P atoms, the more negative the charges of Ni atoms, the stronger the Ni–C interaction, and the easier the cleavage of C–C bond. In a word, $Ni_{12}P_5$ cluster exhibits higher catalytic activity than $Ni_{12}P_6$ cluster toward the hydrodehydration of butyric acid to *n*-butane, owing to its less negative charge of Ni-sites. On the other hand, $Ni_{12}P_6$ cluster displays higher catalytic activity than $Ni_{12}P_5$ cluster toward both direct decarbonylation and dehydration of butyric acid to propylene, because of its more negative charge of Ni-sites.

4. Conclusions

$Ni_{12}P_5$ cluster is preferred to model $Ni_{12}P_5$-based catalyst, with butyric acid as the reactant model, for the deoxygenation of palmitic acid over $Ni_{12}P_5$-based catalyst. The conclusions are as follows.

There exist two main reactions, i.e., Reaction 2 of $C_3H_7COOH + H_2 \rightarrow C_3H_8 + CO + H_2O$ and Reaction 3 of $C_3H_7COOH + 2H_2 \rightarrow C_4H_{10} + 2H_2O$, whereas Reaction 1 of $C_3H_7COOH \rightarrow C_3H_8 + CO_2$ should be ruled out. Propane originates from P-CO-nal with S3 and S4 via butanal intermediate in Reaction 2, where the rate-determining reaction step is related to the formation of HO–H bond. *n*-Butane comes from P-C4-non-ene with S3, S8 and S9 via both butanal and *n*-butanol intermediates and not via butylene in Reaction 3, where the rate-determining reaction step is related to the formation of C–H bond. From the crucial butanal intermediate, decreasing the temperature is profitable to the hydrodehydration to *n*-butane, and increasing the temperature is beneficial to the decarbonylation to propane. In addition, CO roots only in *n*-butanal through decarbonylation, whereas CO_2 is excluded from butyric acid through decarboxylation.

Compared with $Ni_{12}P_6$ cluster, $Ni_{12}P_5$ cluster displays higher catalytic activity toward the hydrodehydration of butyric acid to *n*-butane, thanks to its less negative charge of Ni-sites. Over Ni_xP_y cluster, the fewer the P atoms, the less negative the charge of Ni atoms, the weaker the Ni–H interaction, and the easier the formation of C–H bond. Alternatively, $Ni_{12}P_5$ cluster shows lower catalytic activity toward both direct decarbonylation and dehydration of butyric acid to propylene, because of its less negative charge of Ni-sites. The fewer the P atoms, the less negative the charges of Ni atoms, the weaker the Ni–C interaction, and the more difficult the cleavage of C–C bond.

Supplementary Materials: The following supporting information can be downloaded at: https://www.mdpi.com/article/10.3390/catal12050569/s1, Figure S1: Arrhenius plots of rate constants for the crucial reaction step (F2-IM2 → F2-TS2) in the reaction stage $C_3H_7COOH \rightarrow C_3H_8 + CO_2$ (S2) catalyzed $Ni_{12}P_5$ cluster; Figure S2: Arrhenius plots of rate constants for the crucial reaction step (F3-IM4 → F3-TS4 + C_3H_7CHO) in the reaction stage $C_3H_7COOH + H_2 \rightarrow C_3H_7CHO + H_2O$ (S3) catalyzed by $Ni_{12}P_5$ cluster; Figure S3: Arrhenius plots of rate constants for the crucial reaction step (F4-IM3 → F4-TS3 + CO) in the reaction stage $C_3H_7CHO \rightarrow C_3H_8 + CO$ (S4) catalyzed by $Ni_{12}P_5$ cluster; Figure S4: Arrhenius plots of rate constants for the crucial reaction step (F5-IM4 → F5-TS3 + CO) in the reaction stage $C_3H_7COOH \rightarrow C_2H_5CH_2OH+ CO$ (S5) catalyzed by $Ni_{12}P_5$ cluster; Figure S5: Arrhenius plots of rate constants for the crucial reaction step (F5-IM4 → F7-TS2 + CO) in the reaction stage $C_3H_7COOH \rightarrow CH_3CH=CH_2 + H_2O + CO$ (S5/7a) catalyzed by $Ni_{12}P_5$ cluster; Figure S6: Arrhenius plots of rate constants for the crucial reaction step (F8-IM3 → F8-TS3) in the reaction stage $C_3H_7CHO + H_2 \rightarrow C_3H_7CH_2OH$ catalyzed by $Ni_{12}P_5$ cluster; Figure S7: Arrhenius plots of rate constants for the crucial reaction step (F9-IM3 → F9-TS2) in the reaction stage $C_3H_7CH_2OH + H_2 \rightarrow C_4H_{10} + H_2O$ catalyzed by $Ni_{12}P_5$ cluster; Figure S8: Arrhenius plots of rate constants for the crucial reaction step (F10-IM5 + H_2O → F10-TS1) in the reaction stage $C_3H_7CH_2OH + H_2 \rightarrow C_4H_{10} + H_2O$ (S10a + S10b) catalyzed by $Ni_{12}P_5$ cluster; Figure S9: Arrhenius plots of rate constants for the crucial reaction step (F3-IM4 + H_2 → F8-TS3 + H_2O) in the reaction stage $C_3H_7COOH + 3H_2 \rightarrow C_4H_{10} + 2H_2O$ (S3 + S8 + S9) catalyzed by $Ni_{12}P_5$ cluster; Table S1: Sum of electronic energies (E_t, hartree), free energies (G_0, hartree), sum of electronic and free energies (G_c, hartree), relative energies (G_r, kJ mol^{-1}) and relative energies ($G_r(CO_2\uparrow)$, kJ mol^{-1}, under the experimental condition of 10^{-5} atm pressure of CO_2) of various species with respect to the reactants for the reaction of $C_3H_7COOH \rightarrow C_3H_8 + CO_2$ catalyzed by $Ni_{12}P_5$ cluster at GGA-PBE/DNP, DSPP level; Table S2: Sum of electronic energies (E_t, hartree), free energies (G_0, hartree), sum of electronic and free energies (G_c, hartree) and relative energies (G_r, kJ mol^{-1}) of various species with respect to the reactants for the reaction of $C_3H_7COOH + H_2 \rightarrow C_3H_7CHO + H_2O$ catalyzed by $Ni_{12}P_5$ at GGA-PBE/DNP, DSPP level; Table S3: Sum of electronic energies (E_t, hartree), free energies (G_0, hartree), sum of electronic and free energies (G_c, hartree), relative energies (G_r, kJ mol^{-1}) and relative energies ($G_r(CO\uparrow)$, kJ mol^{-1}, under the experimental condition of 10^{-5} atm pressure of CO) of various species with respect to the reactants for the reaction of $C_3H_7CHO \rightarrow C_3H_8 + CO$ catalyzed by $Ni_{12}P_5$ cluster at GGA-PBE/DNP, DSPP level; Table S4: Sum of electronic energies (E_t, hartree), free energies (G_0, hartree), sum of electronic and free energies (G_c, hartree), relative energies (G_r, kJ mol^{-1}) and relative energies ($G_r(CO\uparrow)$, kJ mol^{-1}, under the experimental condition of 10^{-5} atm pressure of CO) of various species with respect to the reactants for the reaction of $C_3H_7COOH \rightarrow C_2H_5CH_2OH + CO$ catalyzed by $Ni_{12}P_5$ cluster at GGA-PBE/DNP, DSPP level; Table S5: Sum of electronic energies (E_t, hartree), free energies (G_0, hartree), sum of electronic and free energies (G_c, hartree), relative energies (G_r, kJ mol^{-1}) and relative

energies (G_r(CO↑), kJ mol^{-1}, under the experimental condition of 10^{-5} atm pressure of CO) of various species with respect to the reactants for the reaction of $C_2H_5CH_2OH + H_2 \rightarrow C_3H_8 + H_2O$ catalyzed by $Ni_{12}P_5$ cluster at GGA-PBE/DNP, DSPP level; Table S6: Sum of electronic energies (E_t, hartree), free energies (G_0, hartree), sum of electronic and free energies (G_c, hartree), relative energies (G_r, kJ mol^{-1}) and relative energies (G_r(CO↑), kJ mol^{-1}, under the experimental condition of 10^{-5} atm pressure of CO) of various species with respect to the reactants for the reaction of $C_2H_5CH_2OH \rightarrow CH_3CH=CH_2 + H_2O$ catalyzed by $Ni_{12}P_5$ cluster at GGA-PBE/DNP, DSPP level; Table S7: Sum of electronic energies (E_t, hartree), free energies (G_0, hartree), sum of electronic and free energies (G_c, hartree), relative energies (G_r, kJ mol^{-1}) and relative energies (G_r(CO↑), kJ mol^{-1}, under the experimental condition of 10^{-5} atm pressure of CO) of various species with respect to the reactants for the reaction of $CH_3CH=CH_2 + H_2 \rightarrow C_3H_8$ catalyzed by $Ni_{12}P_5$ cluster at GGA-PBE/DNP, DSPP level; Table S8: Sum of electronic energies (E_t, hartree), free energies (G_0, hartree), sum of electronic and free energies (G_c, hartree) and relative energies (G_r, kJ mol^{-1}) of various species with respect to the reactants for the reaction of $C_3H_7CHO + H_2 \rightarrow C_3H_7CH_2OH$ catalyzed by $Ni_{12}P_5$ cluster at GGA-PBE/DNP, DSPP level; Table S9: Sum of electronic energies (E_t, hartree), free energies (G_0, hartree), sum of electronic and free energies (G_c, hartree) and relative energies (G_r, kJ mol^{-1}) of various species with respect to the reactants for the reaction of $C_3H_7CH_2OH + H_2 \rightarrow C_4H_{10} + H_2O$ catalyzed by $Ni_{12}P_5$ cluster at GGA-PBE/DNP, DSPP level; Table S10: Sum of electronic energies (E_t, hartree), free energies (G_0, hartree), sum of electronic and free energies (G_c, hartree) and relative energies (G_r, kJ mol^{-1}) of various species with respect to the reactants for the reaction of $C_3H_7CH_2OH \rightarrow CH_3CH_2CH=CH_2 + H_2O$ catalyzed over $Ni_{12}P_5$ cluster at GGA-PBE/DNP, DSPP level; Table S11: Sum of electronic energies (E_t, hartree), free energies (G_0, hartree), sum of electronic and free energies (G_c, hartree) and relative energies (G_r, kJ mol^{-1}) of various species with respect to the reactants for the reaction of $CH_3CH_2CH=CH_2 + H_2 \rightarrow C_4H_{10}$ catalyzed by $Ni_{12}P_5$ cluster at GGA-PBE/DNP, DSPP level. Refs. [29–34,36] are cited in the Supplementary Materials.

References

1. Ooi, X.Y.; Gao, W.; Ong, H.C.; Lee, H.V.; Juan, J.C.; Chen, W.H.; Lee, K.T. Overview on catalytic deoxygenation for biofuel synthesis using metal oxide supported catalysts. *Renew. Sustain. Energy Rev.* **2019**, *112*, 834–852. [CrossRef]
2. Norouzi, N.; Talebi, S. An overview on the green petroleum production. *Chem. Rev. Lett.* **2020**, *3*, 38–52. [CrossRef]
3. Mahdi, H.I.; Bazargan, A.; McKay, G.; Azelee, N.I.W.; Meili, L. Catalytic deoxygenation of palm oil and its residue in green diesel production: A current technological review. *Chem. Eng. Res. Des.* **2021**, *174*, 158–187. [CrossRef]
4. Itthibenchapong, V.; Srifa, A.; Kaewmeesri, R.; Kidkhunthod, P.; Faungnawakij, K. Deoxygenation of palm kernel oil to jet fuel-like hydrocarbons using Ni-MoS$_2$/γ-Al$_2$O$_3$ catalysts. *Energy Convers. Manag.* **2017**, *134*, 188–196. [CrossRef]
5. Loe, R.; Santillan-Jimenez, E.; Morgan, T.; Sewell, L.; Ji, Y.Y.; Jones, S.; Isaacs, M.A.; Lee, A.F.; Crocker, M. Effect of Cu and Sn promotion on the catalytic deoxygenation of model and algal lipids to fuel-like hydrocarbons over supported Ni catalysts. *Appl. Catal. B* **2016**, *191*, 147–156. [CrossRef]
6. Xin, H.; Guo, K.; Li, D.; Yang, H.Q.; Hu, C.W. Production of high-grade diesel from palmitic acid over activated carbon-supported nickel phosphide catalysts. *Appl. Catal. B* **2016**, *187*, 375–385. [CrossRef]
7. Wongnongwa, Y.; Jungsuttiwong, S.; Pimsuta, M.; Khemthong, P.; Kunaseth, M. Mechanistic and thermodynamic insights into the deoxygenation of palm oils using Ni$_2$P catalyst: A combined experimental and theoretical study. *Chem. Eng. J.* **2020**, *399*, 125586. [CrossRef]
8. Hermida, L.; Abdullah, A.Z.; Mohamed, A.R. Deoxygenation of fatty acid to produce diesel-like hydrocarbons: A review of process conditions, reaction kinetics and mechanism. *Renew. Sustain. Energy Rev.* **2015**, *42*, 1223–1233. [CrossRef]

9. Hongloi, N.; Prapainainar, P.; Prapainainar, C. Review of green diesel production from fatty acid deoxygenation over Ni-based catalysts. *Mol. Catal.* **2022**, *523*, 111696. [CrossRef]

10. Zhang, J.; Huo, X.C.; Li, Y.L.; Strathmann, T.J. Catalytic hydrothermal decarboxylation and cracking of fatty acids and lipids over Ru/C. *ACS Sustain. Chem. Eng.* **2019**, *7*, 14400–14410. [CrossRef]

11. Liu, X.; Yang, M.; Deng, Z.H.; Dasgupta, A.; Guo, Y. Hydrothermal hydrodeoxygenation of palmitic acid over Pt/C catalyst: Mechanism and kinetic modeling. *Chem. Eng. J.* **2021**, *407*, 126332. [CrossRef]

12. Yoosuk, B.; Sanggam, P.; Wiengket, S.; Prasassarakich, P. Hydrodeoxygenation of oleic acid and palmitic acid to hydrocarbon-like biofuel over unsupported Ni-Mo and Co-Mo sulfide catalysts. *Renew. Energy* **2019**, *139*, 1391–1399. [CrossRef]

13. Ansari, K.B.; Gaikar, V.G. Investigating production of hydrocarbon rich bio-oil from grassy biomass using vacuum pyrolysis coupled with online deoxygenation of volatile products over metallic iron. *Renew. Energy* **2019**, *130*, 305–318. [CrossRef]

14. Peroni, M.; Mancino, G.; Baráth, E.; Gutiérrez, O.Y.; Lercher, J.A. Bulk and γ-Al$_2$O$_3$-supported Ni$_2$P and MoP for hydrodeoxygenation of palmitic acid. *Appl. Catal. B* **2016**, *180*, 301–311. [CrossRef]

15. Toba, M.; Abe, Y.; Kuramochi, H.; Osako, M.; Mochizuki, T.; Yoshimura, Y. Hydrodeoxygenation of waste vegetable oil over sulfide catalysts. *Catal. Today* **2011**, *164*, 533–537. [CrossRef]

16. Peroni, M.; Lee, I.; Huang, X.Y.; Baráth, E.; Gutiérrez, O.Y.; Lercher, J.A. Deoxygenation of palmitic acid on unsupported transition-metal phosphides. *ACS Catal.* **2017**, *7*, 6331–6341. [CrossRef]

17. Liu, Y.H.; Yao, L.; Xin, H.; Wang, G.S.; Li, D.; Hu, C.W. The production of diesel-like hydrocarbons from palmitic acid over HZSM-22 supported nickel phosphide catalysts. *Appl. Catal. B* **2015**, *174–175*, 504–514. [CrossRef]

18. Zhou, W.J.; Xin, H.; Yang, H.R.; Du, X.Z.; Yang, R.; Li, D.; Hu, C.W. The deoxygenation pathways of palmitic acid into hydrocarbons on silica-supported Ni$_{12}$P$_5$ and Ni$_2$P catalysts. *Catalysts* **2018**, *8*, 153. [CrossRef]

19. Fu, S.; Wang, Z.M.; Liu, L.J.; Liu, T.H.; Li, D.; Yang, H.Q.; Hu, C.W. Theoretical insight into the deoxygenation molecular mechanism of butyric acid catalyzed by a Ni$_{12}$P$_6$ cluster. *Catal. Sci. Technol.* **2021**, *11*, 6425–6437. [CrossRef]

20. Rundqvist, S.; Larsson, E. The Crystal Structure of Ni$_{12}$P$_5$. *Acta Chem. Scand.* **1959**, *13*, 551–560. [CrossRef]

21. Delley, B. The conductor-like screening model for polymers and surfaces. *Mol. Simul.* **2006**, *32*, 117–123. [CrossRef]

22. Klamt, A. The COSMO and COSMO-RS solvation models. *WIREs Comput. Mol. Sci.* **2018**, *8*, e1338. [CrossRef]

23. Delley, B. From molecules to solids with the DMol^3 approach. *J. Chem. Phys.* **2000**, *113*, 7756–7764. [CrossRef]

24. *Materials Studio*, version 7.0; Accelrys Software Inc.: San Diego, CA, USA, 2013.

25. Perdew, J.P.; Burke, K.; Ernzerhof, M. Generalized gradient approximation made simple. *Phys. Rev. Lett.* **1996**, *77*, 3865–3868. [CrossRef]

26. Perdew, J.P.; Chevary, J.A.; Vosko, S.H.; Jackson, K.A.; Pederson, M.R.; Singh, D.J.; Fiolhais, C. Atoms, molecules, solids, and surfaces: Applications of the generalized gradient approximation for exchange and correlation. *Phys. Rev. B* **1992**, *46*, 6671–6687. [CrossRef]

27. Delley, B. Hardness conserving semilocal pseudopotentials. *Phys. Rev. B* **2002**, *66*, 155125. [CrossRef]

28. Delley, B. An all-electron numerical method for solving the local density functional for polyatomic molecules. *J. Chem. Phys.* **1990**, *92*, 508–517. [CrossRef]

29. Amatore, C.; Jutand, A. Mechanistic and kinetic studies of palladium catalytic systems. *J. Organomet. Chem.* **1999**, *576*, 254–278. [CrossRef]

30. Kozuch, S.; Shalk, S. A Combined kinetic-quantum mechanical model for assessment of catalytic cycles: Application to cross-coupling and heck reactions. *J. Am. Chem. Soc.* **2006**, *128*, 3355–3365. [CrossRef]

31. Kozuch, S.; Shalk, S. Kinetic-quantum chemical model for catalytic cycles: The haber-bosch process and the effect of reagent concentratio. *J. Phys. Chem. A* **2008**, *112*, 6032–6041. [CrossRef]

32. Uhe, A.; Kozuch, S.; Shaik, S. Automatic analysis of computed catalytic cycles. *J. Comput. Chem.* **2011**, *32*, 978–985. [CrossRef] [PubMed]

33. Kozuch, S.; Shalk, S. How to Conceptualize Catalytic Cycles? The Energetic Span Model. *Acc. Chem. Res.* **2011**, *44*, 101–110. [CrossRef] [PubMed]

34. Kozuch, S. Steady State Kinetics of Any Catalytic Network: Graph Theory, the Energy Span Model, the Analogy between Catalysis and Electrical Circuits, and the Meaning of "Mechanism". *ACS Catal.* **2015**, *5*, 5242–5255. [CrossRef]

35. Ren, L.K.; Yang, H.Q.; Hu, C.W. Theoretical study of the catalytic oxidation mechanism of 5-hydroxymethylfurfural to 2,5-diformylfuran by PMo-containing Keggin heteropolyacid. *Catal. Sci. Technol.* **2016**, *6*, 3776–3787. [CrossRef]

36. Wigner, E. Calculation of the Rate of Elementary Association Reactions. *J. Chem. Phys.* **1937**, *5*, 720–725. [CrossRef]